Interpreting U-Nets via Task-Driven Multiscale Dictionary Learning

Tianlin Liu*, Anadi Chaman†, David Belius*, and Ivan Dokmanić*†

*Department of Mathematics and Computer Science, University of Basel.
†Department of Electrical and Computer Engineering, University of Illinois at Urbana-Champaign.

Abstract

U-Nets have been tremendously successful in many imaging inverse problems. In an effort to understand the source of this success, we show that one can reduce a U-Net to a tractable, well-understood sparsity-driven dictionary model while retaining its strong empirical performance. We achieve this by extracting a certain multiscale convolutional dictionary from the standard U-Net. This dictionary imitates the structure of the U-Net in its convolution, scale-separation, and skip connection aspects, while doing away with the nonlinear parts. We show that this model can be trained in a task-driven dictionary learning framework and yield comparable results to standard U-Nets on a number of relevant tasks, including CT and MRI reconstruction. These results suggest that the success of the U-Net may be explained mainly by its multiscale architecture and the induced sparse representation.

1 Introduction

The U-Net (Ronneberger et al., 2015) and related encoder-decoder convolutional neural networks (CNNs) obtain state-of-the-art performance in many imaging inverse problems, especially in computed tomography (CT) and magnetic resonance imaging (MRI) (Chen et al., 2017, Han & Ye, 2018, Zbontar et al., 2018, Hyun et al., 2018, Recht et al., 2020, Kothari et al., 2019). This success has in part been attributed to their ability to represent images at multiple scales, using operations such as convolution, scale-separations (up- and down-sampling), and skip connections. An alternative, well-established approach to imaging problem is based on the sparse representation theory (Elad & Aharon, 2006, Donoho, 2006, Candes et al., 2006, Elad, 2010), where an image is represented as a sparse linear combination of prototype atoms from an over-complete basis called a dictionary. While these two schemes employ very different models, recent studies have shown that they are inherently connected. Notably, Zarka et al. (2020) analyze convolutional multilayer architectures using wavelet scattering (Mallat, 2012, Bruna & Mallat, 2013) and make connections to sparsity; Papyan et al. (2017) argue that convolutions and ReLU nonlinearities in CNNs are closely related to convolutional sparse coding; and Ye et al. (Ye et al., 2018, Ye & Sung, 2019) point out that the encoding and decoding branches of the U-Net are related to the basis element selection process of the convolutional framelets (Yin et al., 2017).

Inspired by these findings, we hypothesize that training the U-Net in a supervised manner is akin to task-driven dictionary learning. More specifically, we conjecture that a significant portion of the U-Net's performance comes from the particular multiscale representation induced by the decoder, and from the sparse representation induced by the encoder. To test this conjecture, we keep the essential structure of the overcomplete representation induced by the U-Net's decoder—convolution, scale separation, and skip connections—but remove nonlinearities, batch normalization, and additive biases to make the architecture linear. In this way, we reduce a U-Net to a sparse representation model with certain multiscale convolutional dictionaries. Surprisingly, as shown in

	LoDoPaB-CT (Leuschner et al., 2019) (challenge fold)		**fastMRI** (Zbontar et al., 2018) (test fold)	
	PSNR (dB)	SSIM	PSNR (dB)	SSIM
Classic U-Net (Ronneberger et al., 2015)	35.87	0.86	33.1	0.76
ISTA U-Net (this work)	36.09	0.86	33.0	0.75

Table 1: The classic U-Net and the sparsity-driven dictionary-based model (dubbed ISTA U-Net) studied in this work perform comparably on two major CT and MRI benchmarks.

Table 1, the resulting task-driven dictionary model performs as well as the U-Net on a number of relevant tasks including CT and MRI. While we do not advocate this model as a replacement for the U-Net, it is favorably interpretable as a composition of sparsity-driven modules, each admitting a well-understood local objective function. Moreover, while the present work is primarily empirical, the U-Net dictionary model may lend itself to theoretical analysis using well-established tools in sparse representations, in turn improving our understanding of the full U-Net.

The rest of the article is organized as follows. We first briefly review the relevant background for the sparse representation model and the U-Net model in Section 2. Section 3 explains how we reduce a U-Net into a dictionary-based model while preserving its essential structure, and how we learn the model from data under the task-driven dictionary learning framework. Section 4 reports experimental results on tasks including single-image super-resolution, CT reconstruction, and MRI reconstruction.

2 Background and Related Work

Sparse representation models. Sparse representation has been extensively studied and widely used in imaging inverse problems (Lustig et al., 2008, Charlety et al., 2013, Liebgott et al., 2013). They are motivated by the idea that many signals, such as images, can be approximated by a linear combination of few elements from a suitable overcomplete basis. Concretely, for a signal of interest[1] $\boldsymbol{x} \in \mathbb{R}^d$, the sparse representation framework posits that we can decompose the signal as $\boldsymbol{x} = \boldsymbol{D}\boldsymbol{\alpha}$, where $\boldsymbol{D} \in \mathbb{R}^{d \times N}$ is an over-complete dictionary of N atoms ($N > d$) and $\boldsymbol{\alpha} \in \mathbb{R}^N$ is a sparse vector with few non-zero entries. Learning a sparse representation model thus comprises two sub-problems: (i) given a dictionary $\boldsymbol{D}$, encode the signal $\boldsymbol{x}$ into a sparse vector $\boldsymbol{\alpha}$ (the sparse coding problem), and (ii) given a set of signals of the form $\boldsymbol{x}$, learn an appropriate dictionary $\boldsymbol{D}$ that sparsifies them (the dictionary learning problem). We briefly review these two problems and show how they are related to neural network models such as CNNs.

The sparse coding problem. The sparse coding problem is often formulated as basis pursuit denoising (Chen & Donoho, 1994) or LASSO regression (Tibshirani, 1996). Most relevant to our work is its formulation with non-negative constraints on the sparse code $\boldsymbol{\alpha}$:

$$\underset{\boldsymbol{\alpha} \geq 0}{\text{minimize}} \quad \frac{1}{2} \|\boldsymbol{x} - \boldsymbol{D}\boldsymbol{\alpha}\|_2^2 + \lambda \|\boldsymbol{\alpha}\|_1 . \tag{1}$$

Here, the first term $\frac{1}{2} \|\boldsymbol{x} - \boldsymbol{D}\boldsymbol{\alpha}\|_2^2$ ensures that the code $\boldsymbol{\alpha}$ yields a faithful representation of $\boldsymbol{x}$, the second term $\lambda \|\boldsymbol{\alpha}\|_1$ controls the sparsity of the code, and the two terms are balanced by a

[1]For ease of notation, we consider 1d vector-valued signals throughout this work, but the formulation can be easily extended to signals of higher dimensions.

parameter $\lambda > 0$. An effective solver for the minimization problem (1) is the iterative shrinkage-thresholding algorithm (ISTA) (Daubechies et al., 2004), which recursively executes the following iteration

$$\boldsymbol{\alpha}^{[k+1]} = \sigma(\boldsymbol{\alpha}^{[k]} + \eta \boldsymbol{D}^T(\boldsymbol{x} - \boldsymbol{D}\boldsymbol{\alpha}^{[k]}) - \eta\boldsymbol{\lambda}), \tag{2}$$

where the upper index $[k]$ denotes the iteration number, η is a step-size parameter, $\boldsymbol{\lambda}$ is a vector whose entries are all λ, and $\sigma(x) \coloneqq \max(x, 0)$ is a component-wise rectifier function.

The task-driven dictionary learning problem. We now briefly recall the task-driven dictionary learning framework (Mairal et al., 2012). Consider a supervised learning setting, in which we are given an input-target data pair $(\boldsymbol{x}, \boldsymbol{y})$, and the goal is to predict $\boldsymbol{y}$ from $\boldsymbol{x}$. For example, $\boldsymbol{x}$ could be a noisy image and $\boldsymbol{y}$ could be a clean image. In the task-driven framework, we proceed by first representing the signal $\boldsymbol{x}$ as a sparse code $\boldsymbol{\alpha}_{\boldsymbol{x},\boldsymbol{D}}$ with respect to the dictionary $\boldsymbol{D}$. One way to achieve this is to let

$$\boldsymbol{\alpha}_{\boldsymbol{x},\boldsymbol{D}} \coloneqq \arg\min_{\boldsymbol{\alpha}\geq 0} \frac{1}{2}\left\|\boldsymbol{x} - \boldsymbol{D}\boldsymbol{\alpha}\right\|_2^2 + \lambda\left\|\boldsymbol{\alpha}\right\|_1, \tag{3}$$

which can be solved by ISTA as described in Equation (1) and (2). Next, we approximate the desired target $\boldsymbol{y}$ using the sparse code $\boldsymbol{\alpha}_{\boldsymbol{x},\boldsymbol{D}}$ through a regression model $f(\cdot, \boldsymbol{w})$ with learnable parameter $\boldsymbol{w}$. For instance, $f(\cdot, \boldsymbol{w})$ could be a linear regression model with weights and biases $\boldsymbol{w}$. In this way, the model output $f(\boldsymbol{\alpha}_{\boldsymbol{x},\boldsymbol{D}}, \boldsymbol{w})$ depends on the regression model parameters $\boldsymbol{w}$ as well as the sparse code $\boldsymbol{\alpha}_{\boldsymbol{x},\boldsymbol{D}}$. The regression parameters $\boldsymbol{w}$ and dictionary $\boldsymbol{D}$ can thus be jointly optimized, for instance, with respect to the quadratic loss objective evaluated on a dataset of M input-target pairs $\{\boldsymbol{x}_i, \boldsymbol{y}_i\}_{i=1}^M$:

$$\underset{\boldsymbol{w},\boldsymbol{D}}{\text{minimize}} \quad \frac{1}{2M}\sum_{i=1}^{M}\left\|f(\boldsymbol{\alpha}_{\boldsymbol{x}_i,\boldsymbol{D}}, \boldsymbol{w}) - \boldsymbol{y}_i\right\|_2^2. \tag{4}$$

Convolutional sparse coding. Our work is in part inspired by the convolutional sparse coding (CSC) model (Yang et al., 2010, Bristow et al., 2013, Papyan et al., 2017), which has gained much attention as it provides a framework of interpreting deep CNNs through the lens of sparse representation. Concretely, Papyan et al. (2017) noticed that if the dictionary $\boldsymbol{D}$ has convolutional structure and if the sparse code $\boldsymbol{\alpha}$ is assumed to be non-negative, a single iteration of ISTA with $\boldsymbol{\alpha}^{[0]}$ initialized as a zero vector and step-size $\eta = 1$ is equivalent to the forward passing a single-layer convolutional network

$$\boldsymbol{\alpha} = \sigma(\boldsymbol{D}^T\boldsymbol{x} + \boldsymbol{b}), \tag{5}$$

where $\boldsymbol{b}$ is a vector whose components are $-\lambda$ (cf. Equation (2)). This single-layer formulation can be extended to characterize a deep CNN of multiple layers. Specifically, the forward-pass of a deep CNN of L-layers can be interpreted to produce the sparse codes $\boldsymbol{\alpha}_1, \cdots, \boldsymbol{\alpha}_L$ sequentially with respect to different dictionaries $\boldsymbol{D}_1, \cdots, \boldsymbol{D}_L$; the back-propagation pass is interpreted to learn these dictionaries $\{\boldsymbol{D}_i\}_{i=1}^L$ in a task-driven way.

The U-Net and its theoretical analysis. The U-Net (Ronneberger et al., 2015) and its variants have been used extensively in solving inverse problems. U-Nets represent images via multi-scale features using a down-sampling branch and an upsampling branch (Figure 1a). In the down-sampling branch, the spatial-resolutions of feature maps are reduced while the number of feature

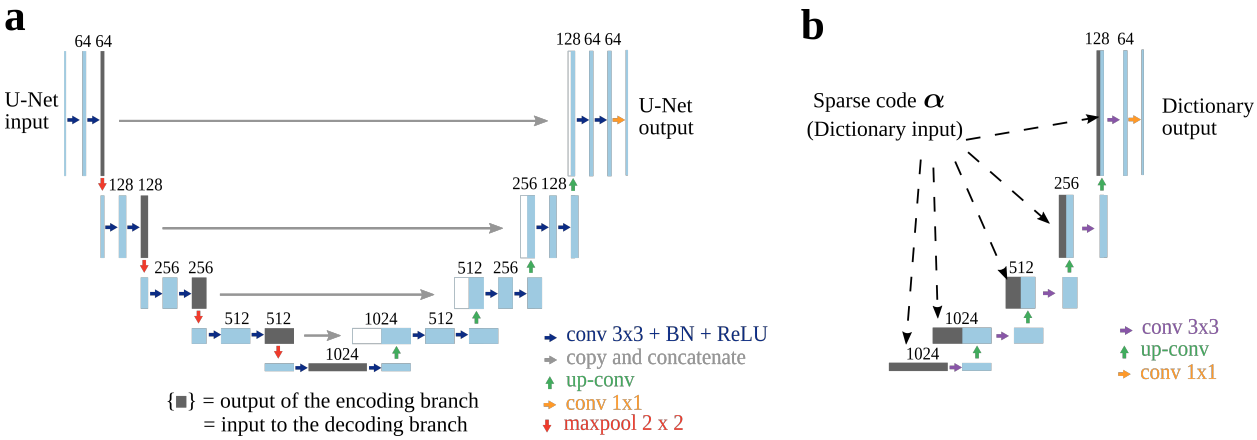

Figure 1: **Schematic illustration of the classic U-Net (left panel) and the dictionary model considered in this work (right panel).** (**a**): The U-Net processes input images using convolution, scale-separation, and skip connections operations in conjunction with ReLU non-linearlities and batch-normalization (BN) modules indicated by colored arrows. The multi-channel feature maps produced by these operations are illustrated as boxes with the channel numbers indicated on the top of these boxes. Dark grey boxes indicate the feature maps produced by the encoding branch of the U-Net, which are sent to the decoding branch either through channel-wise concatenation ("skip connection") or through the bottleneck layer. (**b**): The dictionary considered in this work constitutes the structures of the linear decoder branch of the U-Net with all non-linearlities, batch-normalization, and additive biases removed. Additionally, we remove a convolution operation at each spatial resolution level.

maps is increased; in the decoding branch, these features are re-combined with previous high-resolution features via channel concatenation ("skip connections") and convolution. Heuristically, low-resolution feature maps of a U-Net capture large-scale image properties, whereas the high-resolution feature maps capture more fine-grained image properties (Etmann et al., 2020). In a related line of theoretical work, Ye et al. (Ye et al., 2018, Han & Ye, 2018, Ye & Sung, 2019) proposed to use deep convolutional framelets to study aspects of U-Net-like encoder-decoder CNNs. A key observation they make is that a U-Net model is closely related to convolutional framelets whose frame basis selection depends non-linearly on input data.

3 Method

So far we have presented two well-established approaches to imaging problems: (i) supervised task-driven dictionary learning with sparse representations (ii) supervised learning with the U-Net. Inspired by previous work (Mallat, 2012, Papyan et al., 2017, Ye et al., 2018), here we draw a parallel between these two approaches. We achieve this by reducing a U-Net to a tractable, well-understood sparsity-driven dictionary model.

Encoder-decoder dictionaries. We first introduce a few notations to describe the U-Net's encoding and decoding branches. We denote the encoding branch of the U-Net as a function

$f^{\text{enc}}(\cdot, \boldsymbol{\theta}) : \mathbb{R}^d \to \mathbb{R}^N$ with parameters $\boldsymbol{\theta}$, which maps the input $\boldsymbol{x} \in \mathbb{R}^d$ to some intermediate convolutional feature maps $\boldsymbol{\alpha} = f^{\text{enc}}(\boldsymbol{x}, \boldsymbol{\theta}) \in \mathbb{R}^N$, illustrated as the dark gray boxes in Figure 1a. Note that, for a U-Net, the intermediate feature map dimension N (number of scalar coefficients in $\boldsymbol{\alpha}$) is typically much greater than the image dimension d. These feature maps are then fed into the decoding branch of the U-Net either through skip connections or through the bottleneck layer. To describe this process, we write the decoding branch of the U-Net as a function $f^{\text{dec}}(\cdot, \boldsymbol{\gamma}) : \mathbb{R}^N \to \mathbb{R}^d$ with parameters $\boldsymbol{\gamma}$. That is, the function $f^{\text{dec}}(\cdot, \boldsymbol{\gamma})$ takes the convolutional feature maps produced by the encoding branch and transform them to produce the model output. We can thus write the output produced by a U-Net as

$$\hat{\boldsymbol{y}}(\boldsymbol{x}) \coloneqq f^{\text{dec}}(\boldsymbol{\alpha}, \boldsymbol{\gamma}) = f^{\text{dec}}(f^{\text{enc}}(\boldsymbol{x}, \boldsymbol{\theta}), \boldsymbol{\gamma}).$$

To study the image synthesis process of the U-Net, we focus on the decoding function $f^{\text{dec}}(\cdot, \boldsymbol{\gamma})$. Note that this function synthesizes convolutional feature maps at different spatial scales through skip connections and upsampling. As such, together with the structure of the coefficients $\boldsymbol{\alpha}$ produced by the encoding part it defines an *overcomplete image representation* of the U-Net, similarly to a sparse representation in a dictionary. Indeed, we show in the Appendix that the coefficients $\boldsymbol{\alpha}$ are approximately sparse, or compressible. Additionally, the decoding function is non-linear due to ReLU activations. To separate the bulk of the model structure from its non-linearity, we consider a simpler version of the image synthesis process by removing all non-linearities, batch normalization, and additive biases from the function $f^{\text{dec}}(\cdot, \boldsymbol{\gamma})$, as shown in Figure 1b. The resulting function is then simply a linear transformation, sharing the essential ingredients of convolution, scale separation, and skip connections with the U-Net decoding branch. This linear transformation is written as a dictionary $\boldsymbol{D}_{\boldsymbol{\gamma}} \in \mathbb{R}^{d \times N}$ with atoms $\boldsymbol{\gamma}$, to which we refer as the decoder dictionary. A mathematical definition of the decoder dictionary $\boldsymbol{D}_{\boldsymbol{\gamma}}$ through convolution and upsampling is provided in the Appendix A.

With a given decoder dictionary $\boldsymbol{D}_{\boldsymbol{\gamma}}$ to describe the image synthesis process, we next consider how to infer an associated sparse code $\boldsymbol{\alpha}$, so that $\boldsymbol{D}_{\boldsymbol{\gamma}}\boldsymbol{\alpha}$ is a good approximation of the image we wish to model. In a supervised learning setting where the input image $\boldsymbol{x}$ is given, it is natural to interpret $\boldsymbol{\alpha}$ as an encoded representation of $\boldsymbol{x}$. Since the encoding must produce a coefficient vector whose structure is compatible with $\boldsymbol{\alpha}$, we endow an encoder dictionary $\boldsymbol{D}_{\boldsymbol{\theta}} \in \mathbb{R}^{d \times N}$ with the same structure of $\boldsymbol{D}_{\boldsymbol{\gamma}}$ albeit with a different set of atoms $\boldsymbol{\theta}$. This setup is analogous to U-Net's encoding and decoding branches: the encoder and decoder dictionaries $\boldsymbol{D}_{\boldsymbol{\theta}}$ and $\boldsymbol{D}_{\boldsymbol{\gamma}}$ are employed to process input signals and produce output signals, respectively. Specifically, we leverage these dictionaries to impose sparsity priors on data: We posit that each input-target data pair $(\boldsymbol{x}, \boldsymbol{y}) \in \mathbb{R}^d \times \mathbb{R}^d$ admits a shared underlying sparse code $\boldsymbol{\alpha}$ with respect to the encoder and decoder dictionaries:

$$\boldsymbol{D}_{\boldsymbol{\theta}}\boldsymbol{\alpha} \approx \boldsymbol{x} \quad \text{and} \quad \boldsymbol{D}_{\boldsymbol{\gamma}}\boldsymbol{\alpha} \approx \boldsymbol{y} \quad \text{for } \boldsymbol{\alpha} \text{ sparse.} \tag{6}$$

The parallels between the two image models are summarized in Table 2. We now proceed to describe how to exploit the sparse prior (6) to solve a supervised learning task.

The task-driven dictionary learning objective. Under the task-driven framework introduced in Section 2, we tackle a supervised learning problem by performing sparse coding and dictionary learning. Concretely, we solve the following bi-level minimization problem over a dataset of M

	Encoding	Decoding
U-Net	$\boldsymbol{\alpha} \coloneqq f^{\text{enc}}(\boldsymbol{x}, \boldsymbol{\theta})$	$\hat{\boldsymbol{y}} \coloneqq f^{\text{dec}}(\boldsymbol{\alpha}, \boldsymbol{\gamma})$
ISTA U-Net	$\boldsymbol{\alpha} \coloneqq \text{ISTA}(\boldsymbol{x}, \boldsymbol{D}_{\boldsymbol{\theta}})$	$\hat{\boldsymbol{y}} \coloneqq \boldsymbol{D}_{\boldsymbol{\gamma}}\boldsymbol{\alpha}$

Table 2: **A comparison between the branches of the U-Net and ISTA U-Net.** Here, $\text{ISTA}(\boldsymbol{x}, \boldsymbol{D}_{\boldsymbol{\theta}})$ corresponds to ISTA iterations described in Equation (8).

input-target pairs $\{\boldsymbol{x}_i, \boldsymbol{y}_i\}_{i=1}^M$:

$$\begin{aligned} \underset{\{\boldsymbol{\theta},\boldsymbol{\gamma}\},\boldsymbol{\lambda}>0}{\text{minimize}} \quad & \frac{1}{2M}\sum_{i=1}^{M} \|\boldsymbol{D}_{\boldsymbol{\gamma}}\boldsymbol{\alpha}_{\boldsymbol{x}_i,\boldsymbol{\theta}} - \boldsymbol{y}_i\|_2^2 \\ \text{where} \quad & \boldsymbol{\alpha}_{\boldsymbol{x}_i,\boldsymbol{\theta}} = \underset{\boldsymbol{\alpha}\geq 0}{\arg\min}\, \frac{1}{2}\|\boldsymbol{D}_{\boldsymbol{\theta}}\boldsymbol{\alpha} - \boldsymbol{x}_i\|_2^2 + \|\boldsymbol{\lambda} \odot \boldsymbol{\alpha}\|_1, \end{aligned} \tag{7}$$

for $\odot$ being the Hadamard product (cf., Equation (3) and Equation (4)). In plain words, the objective of Equation (7) aims to minimize the discrepancy between the ground-truth signal $\boldsymbol{y}$ and the model prediction $\boldsymbol{D}_{\boldsymbol{\gamma}}\boldsymbol{\alpha}_{\boldsymbol{x},\boldsymbol{\theta}}$, where the latter is a signal synthesized from a sparse code $\boldsymbol{\alpha}_{\boldsymbol{x},\boldsymbol{\theta}}$ via the decoder dictionary $\boldsymbol{D}_{\boldsymbol{\gamma}}$; the code $\boldsymbol{\alpha}_{\boldsymbol{x},\boldsymbol{\theta}}$, defined through the argmin function in Equation (7) is a sparse representation of the input image $\boldsymbol{x}$ with respect to the encoder dictionary $\boldsymbol{D}_{\boldsymbol{\theta}}$ under a Lasso-like objective. Note that here the argmin function in Equation (7) is slightly different from the traditional Lasso objective for non-negative sparse coding in that the sparsity-controlling parameter $\boldsymbol{\lambda}$ here is a vector, weighting codes component-wise. The role of $\boldsymbol{\lambda}$ will be explained shortly.

ISTA U-Net as an unrolled optimizer. To solve the bi-level task-driven dictionary learning problem (7), we use an unrolled optimization approach, which constitutes a sparse coding module and a dictionary-based synthesis module. First, the sparse coding module uses the dictionary $\boldsymbol{D}_{\boldsymbol{\theta}}$ to transform the input $\boldsymbol{x}$ into a sparse code $\boldsymbol{\alpha}_{\boldsymbol{x},\boldsymbol{\theta}}$. This is achieved by unrolling a fixed T number of ISTA iterations:

$$\boldsymbol{\alpha}_{\boldsymbol{x},\boldsymbol{\theta}}^{[t+1]} \coloneqq \sigma\Big(\boldsymbol{\alpha}_{\boldsymbol{x},\boldsymbol{\theta}}^{[t]} + \eta\boldsymbol{D}_{\boldsymbol{\theta}}^{\top}\big(\boldsymbol{x} - \boldsymbol{D}_{\boldsymbol{\theta}}\boldsymbol{\alpha}_{\boldsymbol{x},\boldsymbol{\theta}}^{[t]}\big) - \eta\boldsymbol{\lambda}\Big), \tag{8}$$

where $t = 0, \ldots, T-1$ is the iteration index and η is a step-size parameter. Next, the synthesis module generates the model output by linearly combining atoms in the decoder dictionary $\boldsymbol{D}_{\boldsymbol{\gamma}}$ with the inferred sparse code $\boldsymbol{\alpha}_{\boldsymbol{x},\boldsymbol{\theta}}^{[T]}$:

$$\widehat{\boldsymbol{y}}_{\boldsymbol{\theta},\boldsymbol{\gamma}}(\boldsymbol{x}) \coloneqq \boldsymbol{D}_{\boldsymbol{\gamma}}\boldsymbol{\alpha}_{\boldsymbol{x},\boldsymbol{\theta}}^{[T]}, \tag{9}$$

Putting Equation (8) and (9) together yields a computational graph which we call ISTA U-Net. We note that our ISTA U-Net described above is an instance of a *optimization-driven network* (Lecouat et al., 2020), which is a network explicitly derived by unrolling an optimization algorithm. As such, the model is interpretable in the sense that each module of the model admits a mathematically principled local objective function, a characteristic typically not possessed by end-to-end trained deep networks.

Training the ISTA U-Net. An ISTA U-Net can be trained from data following the standard supervised learning pipeline. Here we provide a concrete recipe adopted by our work:

1. **Dictionary initialization.** Randomly initialize the encoder and decoder dictionaries $\boldsymbol{D}_{\boldsymbol{\theta}}$ and $\boldsymbol{D}_{\boldsymbol{\gamma}}$.

2. **Model forward pass.** This amounts to sequentially execute the sparse coding module of Equation (8) and the dictionary-based synthesis module of Equation (9).

3. **Task-driven dictionary learning.** For a mini-batch of input-target pairs $\{(\boldsymbol{x}_i, \boldsymbol{y}_i)\}_{i=1}^{n_B}$ of n_B samples, minimize the mean square error between the output and target

$$\frac{1}{2n_B} \sum_{i=1}^{n_B} \|\widehat{\boldsymbol{y}}_{\boldsymbol{\theta},\boldsymbol{\gamma}}(\boldsymbol{x}_i) - \boldsymbol{y}_i\|_2^2$$

   with gradient descent on the encoder dictionary $\boldsymbol{D}_{\boldsymbol{\theta}}$, decoder dictionary $\boldsymbol{D}_{\boldsymbol{\gamma}}$, sparsity-inducing parameter $\boldsymbol{\lambda}$, and step-size parameter η.

Before presenting the experiments, we offer some general remarks pertaining to the implementation of the learning procedure outlined above. Note that the sparse code $\boldsymbol{\alpha}^{[t]}$ for each t in Equation (8) is a collection of multi-channel convolutional feature maps. Throughout this work, we tie components of sparsity inducing term $\boldsymbol{\lambda}$ if these components are applied to the same convolutional feature map. We initialize each sparse code $\boldsymbol{\alpha}_{\boldsymbol{x},\boldsymbol{\theta}}^{[0]}$ as a collection of all-zero tensors. The ISTA step-size parameter η is initialized as the inverse of the dominant eigenvalue of the matrix $\boldsymbol{D}_{\boldsymbol{\theta}}^{\top}\boldsymbol{D}_{\boldsymbol{\theta}}$, which can be approximated using a power iteration method (details in Appendix B) and we set it to be learnable during supervised training. Additionally, we follow Lecouat et al. (2020) and use the "untied parameters" trick for the sparse coding step: Instead of directly using Equation (8), we use another dictionary $\boldsymbol{D}_{\boldsymbol{\kappa}}$, having the same structure of $\boldsymbol{D}_{\boldsymbol{\theta}}$ albeit with a different set of atoms $\boldsymbol{\kappa}$, as a learnable pre-conditioner and compute

$$\boldsymbol{\alpha}^{[t+1]} := \sigma\Big(\boldsymbol{\alpha}^{[t]} + \eta \boldsymbol{D}_{\boldsymbol{\kappa}}^{\top}\big(\boldsymbol{x} - \boldsymbol{D}_{\boldsymbol{\theta}}\boldsymbol{\alpha}^{[t]}\big) - \eta\boldsymbol{\lambda}\Big). \tag{10}$$

The dictionary $\boldsymbol{D}_{\boldsymbol{\kappa}}$ is then jointly optimized together with $\boldsymbol{D}_{\boldsymbol{\theta}}$ and $\boldsymbol{D}_{\boldsymbol{\gamma}}$ using gradient descent.

4 Experiments

We numerically compared the U-Net and ISTA U-Net on tasks including super-resolution, CT reconstruction, and MRI reconstruction. Throughout this section, we use "classic U-Net" to refer the U-Net architecture originally proposed in Ronneberger et al. (2015), which is illustrated in Figure 1a. For CT and MRI experiments, we also included modified U-Nets and other deep network baselines for comparison purposes, which will be described in the corresponding subsections. The ISTA U-Net architecture used always mimics the classic U-Net in its encoder and decoder dictionaries (Figure 1b). All hyper-parameter choices for the experiments are provided in Appendix C. The code to reproduce our experimentsis available at https://github.com/liutianlin0121/ISTA-U-Net.

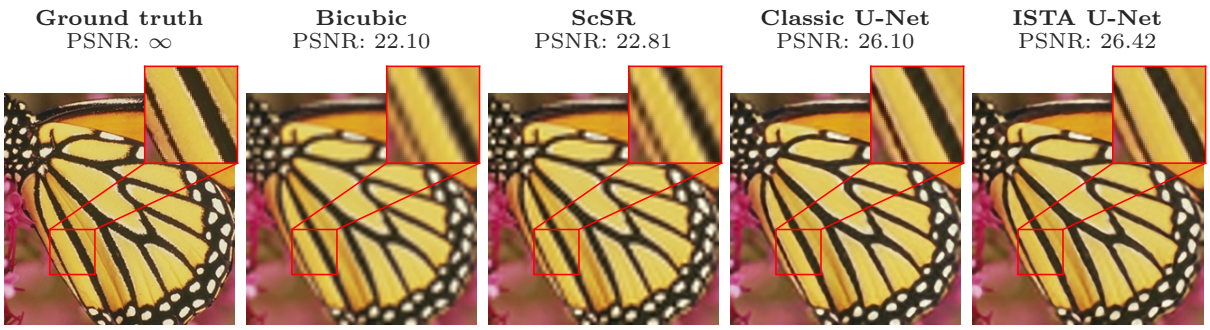

Figure 2: **Reconstructions of a test sample from the Set-5 dataset.**

	Set-5	Set-14	B-100	Urban-100
ScSR (Yang et al., 2010)	29.07	26.40	26.61	24.02
A+ (Timofte et al., 2015)	30.17	26.94	26.81	24.29
CSC (Gu et al., 2015)	30.29	26.91	26.82	24.36
Classic U-Net	30.52	27.43	27.04	24.68
ISTA U-Net	30.90	27.77	27.07	24.71

Table 3: **Performance on the single-image super-resolution task with a scaling factor of four.**

4.1 Super-resolution

Single-image super-resolution is one of the most classical imaging inverse problems, which aims to recover a high-resolution (HR) image from its degraded, low-resolution (LR) version. Sparse representation models have been extensively studied to tackle this task, yielding near state-of-the-art results when the training data set is relatively small and the degradation level relatively mild (Yang et al., 2010, Timofte et al., 2015, Gu et al., 2015). However, deep CNNs trained on abundant data have shown to deliver improved results, especially on severely degraded images (Dong et al., 2016, Kim et al., 2016, Lim et al., 2017). Here we applied the U-Net and ISTA U-Net on this classical task in the interest of benchmarking their results in comparison to well-established sparse representation baselines. Note that our motivation here is not to achieve the state-of-the-art result – both the U-Net and ISTA U-Net architectures were not adapted to this task; rather, we have sought to evaluate both models on this extensively studied problem and see if these "out-of-the-box" models could favorably compete with existing baselines.

To that end, we followed the protocol of previous work (Schulter et al., 2015, Kim et al., 2016, Lai et al., 2017) and used 291 images therein to train the classic U-Net and ISTA U-Net. LR images were prepared by down-scaling HR images by a factor of four. We used bicubic interpolated images up-scaled from LR images as model inputs and HR images as model targets. The trained models were evaluated on standard datasets including Set-14 (Zeyde et al., 2010), Set-5 (Bevilacqua et al., 2012), B-100 (Martin et al., 2001), and Urban-100 (Huang et al., 2015).

Table 3 shows the performance of the trained models. We found that both classic U-Nets and U-Nets outperform well-established sparse representing baseline methods such as ScSR, A+, and CSC.

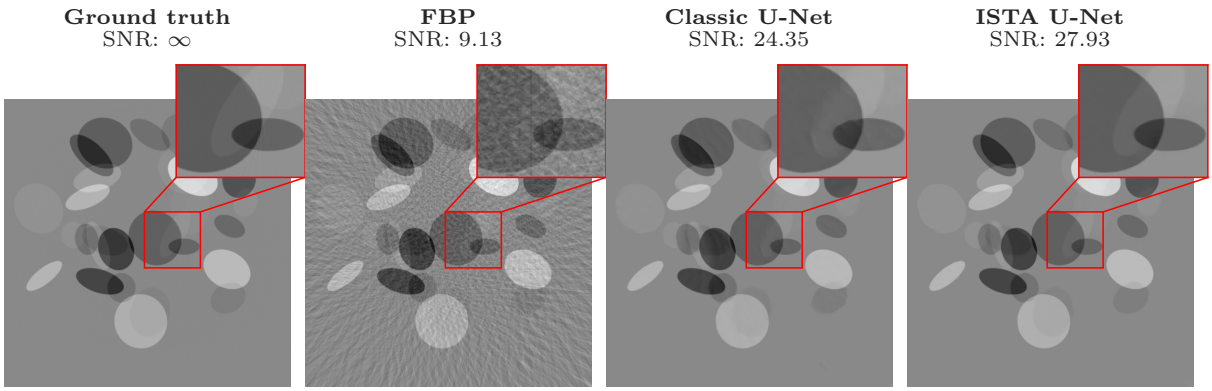

Figure 3: **Reconstructions of a test sample from the ellipsoid phantom dataset**.

	SNR (dB)
FBP	8.44
TV	27.69
Classic U-Net	23.84
ISTA U-Net	27.02

Table 4: **Performance on the ellipsoid phantom test data.**

Figure 2 shows visual comparison between models. We noted that, however, the performance of U-Net and ISTA U-Net is worse than state-of-the-art deep networks specialized in super-resolution, typically by around 1 dB (Dong et al., 2016, Kim et al., 2016, Lim et al., 2017).

4.2 CT reconstruction

We proceed to present experimental results on the computed tomography (CT) reconstruction task, which aims to recover images from their sparse-view sinograms. We used two benchmark datasets: the ellipsoid phantom (Jin et al., 2017) and the LoDoPaB-CT datasets (Leuschner et al., 2019).

The ellipsoid phantom dataset. This dataset contains 500 images of random ellipses together with their associated filtered back-projection (FBP) (Shepp & Logan, 1974) from uniformly sub-sampled sinogram measurements by a factor of twenty. As in Jin et al. (2017), we used 475 images as training images, the remaining 25 images as testing images, and used signal-to-noise ratio (SNR) to measure the reconstruction results. The SNR between a prediction $\hat{\boldsymbol{y}}$ and a ground-truth signal $\boldsymbol{y}$ is defined by

$$\mathrm{SNR}(\hat{\boldsymbol{y}}, \boldsymbol{y}) \coloneqq \sup_{a,b\in\mathbb{R}} 20 \log_{10} \left(\frac{\|\boldsymbol{y}\|_2}{\|\boldsymbol{y} - a\hat{\boldsymbol{y}} + b\|_2} \right).$$

Table 4 and Figure 3 show the reconstruction results on the test images. We see that the FBP reconstruction exhibited pronounced streak-like artifacts. These artifacts were significantly

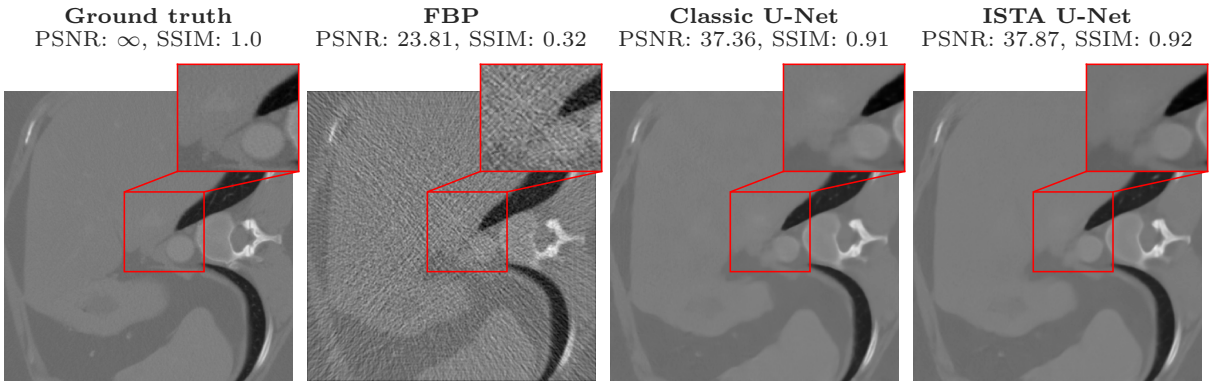

Figure 4: **Reconstructions of a test sample from the LoDoPaB-CT dataset.**

	PSNR (dB)	SSIM
FBP	30.37	0.74
TV Regularization	32.95	0.80
DIP + TV (Baguer et al., 2020)	34.44	0.81
iRadonMap (He et al., 2020)	31.23	0.76
Learned GD (Adler & Öktem, 2017)	34.36	0.81
Learned PD (Adler & Öktem, 2018)	35.73	0.84
Small U-Net	35.48	0.84
Classic U-Net	35.71	0.84
ISTA U-Net	35.83	0.84

Table 5: **Performance on the LoDoPaB-CT test data.** All numerical results except the classic U-Net and ISTA U-Net are taken from Baguer et al. (2020, Appendix B), which were evaluated on the first 100 test samples. Here, "Small U-Net" refers to the U-Net used in Baguer et al. (2020) and Leuschner (2020), which is a slightly down-scaled version of the classic U-Net.

reduced by TV, U-Net, and ISTA U-Net methods. Numerically, TV delivered the best SNR, which is a reasonable result as TV should be optimal for reconstructing piecewise constant images (Jin et al., 2017, Chambolle, 2004). ISTA U-Net achieved a better SNR than Classic U-Net, but both reconstructions were visually comparable (Figure 3).

The LoDoPaB-CT dataset. This dataset contains more than 40000 pairs of human chest CT images and their simulated low photon count measurements. We used the default dataset split, with 35820 training samples, 3522 validation samples, 3553 test samples as recommended in Leuschner et al. (2019). As in Jin et al. (2017), to train U-Nets and ISTA U-Nets, we first transformed the sinogram measurements back to the image space using FBP, which was the only pre-processing we performed. Table 5 and Figure 4 show the reconstruction results on the test set. The U-Net variants all achieved superior results. Importantly, ISTA U-Net replicated U-Net's strong performance in this task.

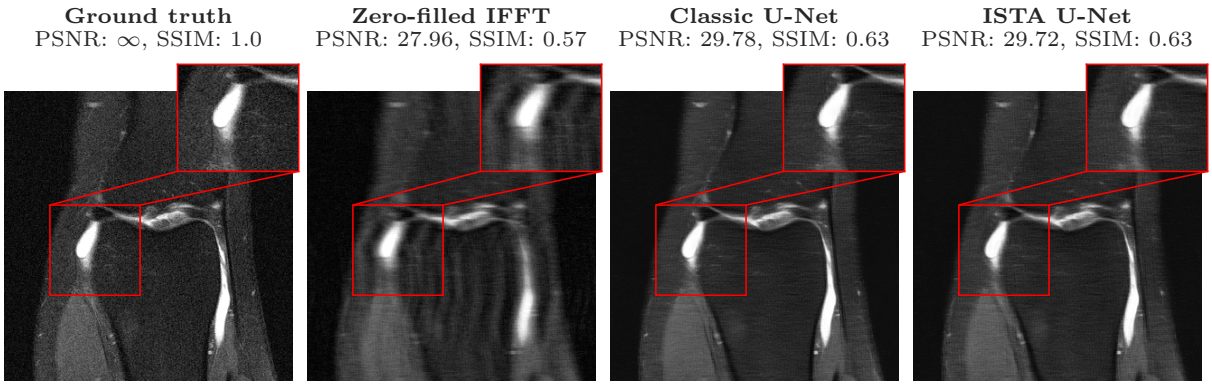

Figure 5: **Reconstructions of a test sample from the fastMRI single-coil knee dataset.**

	#Params	NMSE		PSNR		SSIM	
		PD	PDFS	PD	PDFS	PD	PDFS
TV	-	0.287	0.09	31.4	27.7	0.645	0.494
U-Net-32	3.35M	0.0161	0.0531	33.78	29.90	0.81	0.631
U-Net-64	13.39M	0.0157	0.0528	33.90	29.9	0.813	0.633
U-Net-128	53.54M	0.0154	0.0525	34.01	29.95	0.815	0.634
U-Net-256	214.16M	0.0154	0.0525	34.00	29.95	0.815	0.636
Classic U-Net	31M	0.0153	0.0522	34.05	29.98	0.8142	0.6331
ISTA U-Net	55M	0.0157	0.0527	33.91	29.94	0.8115	0.6321

Table 6: **Performance on fastMRI single-coil knee validation data**. Results are collected from (Zbontar et al., 2018) except Classic U-Net and ISTA U-Net. The U-Net-32 model refers to a U-Net variant defined in (Zbontar et al., 2018) whose output after the first convolution has 32 channels. Other models are defined similarly.

We additionally tested classic U-Net and ISTA U-Net on the challenge-fold of the LoDoPaB-CT dataset, which contains 3678 images with ground-truth hidden from the public. The evaluation on this challenge dataset is restricted through an online submission system[2]. There, ISTA U-Net results are currently ranked as the second-best on the leaderboard, and U-Net results are ranked as the third best. These results were shown in Table 1.

4.3 MRI reconstruction

We further considered the task of accelerated MRI reconstruction using the fastMRI dataset (Zbontar et al., 2018) procured by Facebook and NYU. Specifically, we used the single-coil knee dataset with a 4-fold acceleration factor. This dataset contains 973 volumes or 34742 slices in the training set, 199 volumes or 7135 slices in the validation set, and 108 volumes or 3903 slices in the test set.

[2] https://lodopab.grand-challenge.org/challenge/

	#Params	NMSE		PSNR		SSIM	
		PD	PDFS	PD	PDFS	PD	PDFS
TV	-	0.0221	0.0716	33.1	28.5	0.7036	0.5096
U-Net-256	214.16M	0.0115	0.0414	35.9	30.8	0.8618	0.6680
Classic U-Net	31M	0.0122	0.0418	35.6	30.8	0.8567	0.8649
ISTA U-Net	55M	0.0127	0.0422	35.4	30.7	0.8537	0.6637

Table 7: **Performance on single-coil knee test data**. Results are collected from the fastMRI public leaderboard.

The ground-truth images in the test set are not provided to the public and the evaluation must be made through the fastMRI online submission system[3].

Following the training protocol of Zbontar et al. (2018), we first transformed undersampled k-space measurements into the image space using zero-filled Inverse Fast Fourier Transform (IFFT) and used the transformed images as inputs to the U-Net and ISTA U-Net. Consistent with previous work Zbontar et al. (2018), we found that U-Nets deliver exceptional performance. Table 6 shows the results on validation samples. Importantly, recapitulating our previous findings, this remarkable empirical performance was well-captured by the ISTA U-Net, yielding visually indistinguishable results (Figure 5). We next evaluated the classic U-Net and the ISTA U-Net on test samples through the fastMRI submission system. On test data, both the classic U-Net and ISTA U-Net produced results comparable to the best-performing U-Net result provided by the fastMRI challenge organizer while having many fewer parameters (Table 7). This highlights the fact that the ISTA U-Net qualitatively reproduces the U-Net's performance in tasks in which the latter excels.

4.4 The compressibility of U-Net and ISTA U-Net feature maps

Beyond than observing conspicuous similarities in U-Net and ISTA U-Net's empirical performance, we have probed their internal representations. We found that convolutional feature maps of the U-Net and the ISTA U-Net are similarly compressible in the sense that the sorted magnitudes of the coefficients $\boldsymbol{\alpha}$ decay at a similar rate. This suggests that both models fundamentally exploit a sparse expansion in a certain overcomplete image representation, nonlinear for the U-Net and linear for the ISTA U-Net. The detailed results are reported in Appendix D.

5 Discussion

This work constitutes an effort to understand the highly successful U-Net model. To that end, we reduced a U-Net model to a sparsity-driven dictionary model by extracting its essential structures and removing nonlinearities. We verified that, when the extracted model is optimized in a task-driven dictionary learning framework, it replicates the U-Net's empirical success in major imaging inverse problems.

Beyond empirical performance, we believe that the interpretability of the derived model is showing the way towards a theoretical analysis of a successful deep learning model. The interpretability

[3] https://fastmri.org/

and theoretical backing of sparsity-driven models may also be desirable in critical applications such as medical imaging. An interpretable model needs to consist of components whose objectives and functionality are mathematically well-understood. We take an empirical step in this direction by reducing the U-Net to a model comprising two modules with well-understood objectives, one implementing sparse coding and the other dictionary-based synthesis.

This work opens up new possibilities for unifying the CNN approach and the sparse representation approach for solving inverse problems, following the spearheading results of Papyan et al. (2017). Indeed, throughout this work we have consistently observed that U-Net and ISTA U-Net yield reconstructions that are within half a dB in PSNR. This striking similarity might indicate that both models are fundamentally governed by a shared structured image model.

Acknowledgments

We thank Johannes Leuschner for helpful discussions regarding the LoDoPaB-CT dataset. This work was supported by the European Research Council Starting Grant 852821—SWING. Numerical experiments were partly performed at the sciCORE (http://scicore.unibas.ch/) scientific computing center at the University of Basel.

Appendix A The definition of the decoder dictionary

In the main text we have illustrated the architecture of a classic U-Net (Figure 1a) and a decoder dictionary (Figure 1b). There, we referred to the decoder dictionary as the decoding branch of a standard U-Net with all ReLU activations, batch-normalization, and some convolution operations removed. Here we provide a formal definition of the decoder dictionary through convolution and upsampling. While in the main text we assumed that signals are vector-valued, in this section, we extend our setting to handle tensor-valued signals with multiple channels such as RGB-colored images. To that end, we first consider single-input single-output (SISO) operations whose input and output are 2D signals having a single channel. We follow by considering multiple-input multiple-output (MIMO) operations whose input and output are 3D tensors having multiple channels.

A.1 SISO convolution and transposed convolution

Let $\boldsymbol{\xi} \in \mathbb{R}^{H\times W}$ be a 2D signal with height H and width W. We regard the signal as a function defined on the discrete domain $\{1,\dots,H\}\times\{1,\dots,W\}$. With standard zero padding, we extend the domain of $\boldsymbol{\xi}$ to $\mathbb{Z}\times\mathbb{Z}$. The notation $\boldsymbol{\xi}[i,j]$ represents the value of the function $\boldsymbol{\xi}$ at the coordinate (i,j).

SISO convolution Given a 2D signal $\boldsymbol{\xi} \in \mathbb{R}^{H\times W}$ and parameters $\boldsymbol{w} \in \mathbb{R}^{3\times 3}$, the 3-by-3 convolution of $\boldsymbol{\xi}$ and $\boldsymbol{w}$ is defined as

$$(\boldsymbol{w} * \boldsymbol{\xi})[i,j] = \sum_{p=-1}^{1}\sum_{q=-1}^{1} \boldsymbol{\xi}[i+p, j+q]\cdot \boldsymbol{w}[p,q]. \tag{11}$$

SISO transposed convolution A transposed convolution of a U-Net consists of a bed-of-nails up-sampling by a factor of two followed by a 2-by-2 convolution. The bed-of-nails up-sampling of a signal $\boldsymbol{\xi}$ is realized by interleaving zeros in the signal, which can be written as $\boldsymbol{\xi} \otimes \left[\begin{smallmatrix}0 & 0\\ 0 & 1\end{smallmatrix}\right]$ with $\otimes$ denoting the Kronecker product. The 2-by-2 convolution between filter $\boldsymbol{v} \in \mathbb{R}^{2\times 2}$ and signal $\boldsymbol{\xi} \in \mathbb{R}^{H\times W}$ is written as

$$(\boldsymbol{v} \circledast \boldsymbol{\xi})[i,j] = \sum_{p=0}^{1}\sum_{q=0}^{1} \boldsymbol{\xi}[i+p, j+q]\cdot \boldsymbol{v}[p,q]. \tag{12}$$

Putting these together, we have the following definition for a transposed convolution.

Definition 1. A transposed convolution $\mathcal{U}_{\boldsymbol{v}}$ parameterized by the convolutional filter $\boldsymbol{v} \in \mathbb{R}^{2\times 2}$ is a map defined by

$$\begin{aligned}\mathcal{U}_{\boldsymbol{v}}\colon \mathbb{R}^{n\times n} &\to \mathbb{R}^{2n\times 2n}\\ \boldsymbol{\xi} &\mapsto \boldsymbol{v} \circledast (\boldsymbol{\xi} \otimes \left[\begin{smallmatrix}0 & 0\\ 0 & 1\end{smallmatrix}\right]).\end{aligned}$$

We show a technical result that simplifies the up-sampling calculation.

Proposition 1. Let $\boldsymbol{v} \in \mathbb{R}^{2\times 2}$ be a matrix and let $\bar{\boldsymbol{v}}$ be its vertically and horizontally flipped version, i.e., $\bar{\boldsymbol{v}}[i,j] = \boldsymbol{v}[3-i, 3-j]$ for $(i,j) \in \{1,2\}\times\{1,2\}$. Let $\boldsymbol{\xi} \in \mathbb{R}^{n\times n}$ be a matrix with dimension $n \geq 2$. Then the following equation holds:

$$\mathcal{U}_{\boldsymbol{v}}(\boldsymbol{\xi}) = \boldsymbol{\xi} \otimes \bar{\boldsymbol{v}}. \tag{13}$$

Proof. Observe that the result of LHS and RHS are both $2n$-by-$2n$ matrices, each composed of $n \times n$ number of 2-by-2 sub-matrices. It is enough to show that each 2-by-2 sub-matrix of the LHS equals that of the RHS if they have the same position indices.

We first expand the RHS. By definition of Kronecker product, we have

$$\boldsymbol{\xi} \otimes \bar{\boldsymbol{v}} = \begin{bmatrix} \boldsymbol{\xi}[1,1]\bar{\boldsymbol{v}} & \cdots & \boldsymbol{\xi}[1,n]\bar{\boldsymbol{v}} \\ \vdots & \ddots & \vdots \\ \boldsymbol{\xi}[n,1]\bar{\boldsymbol{v}} & \cdots & \boldsymbol{\xi}[n,n]\bar{\boldsymbol{v}} \end{bmatrix} \in \mathbb{R}^{2n \times 2n},$$

where the (i,j)-th 2-by-2 sub-matrix of $\boldsymbol{\xi} \otimes \bar{\boldsymbol{v}}$ has the form

$$\boldsymbol{\xi}[i,j]\bar{\boldsymbol{v}} = \begin{bmatrix} \boldsymbol{\xi}[i,j] \cdot \boldsymbol{v}[2,2] & \boldsymbol{\xi}[i,j] \cdot \boldsymbol{v}[2,1] \\ \boldsymbol{\xi}[i,j] \cdot \boldsymbol{v}[1,2] & \boldsymbol{\xi}[i,j] \cdot \boldsymbol{v}[1,1] \end{bmatrix}, \tag{14}$$

for each $(i,j) \in \{1, \cdots, n\} \times \{1, \cdots, n\}$.

For the LHS, we have $\mathcal{U}_{\boldsymbol{v}}(\boldsymbol{\xi}) = \boldsymbol{v} \circledast (\boldsymbol{\xi} \otimes \left[\begin{smallmatrix} 0 & 0 \\ 0 & 1 \end{smallmatrix}\right])$ by definition. Writing out the Kronecker product, we see that the (i,j)-th 2-by-2 sub-matrix of the LHS has the form

$$\boldsymbol{v} \circledast \begin{bmatrix} 0 & 0 & 0 \\ 0 & \boldsymbol{\xi}[i,j] & 0 \\ 0 & 0 & 0 \end{bmatrix} = \begin{bmatrix} \boldsymbol{\xi}[i,j] \cdot \boldsymbol{v}[2,2] & \boldsymbol{\xi}[i,j] \cdot \boldsymbol{v}[2,1] \\ \boldsymbol{\xi}[i,j] \cdot \boldsymbol{v}[1,2] & \boldsymbol{\xi}[i,j] \cdot \boldsymbol{v}[1,1] \end{bmatrix}, \tag{15}$$

for each $(i,j) \in \{1, \cdots, n\} \times \{1, \cdots, n\}$. Comparing Equation (14) and Equation (15), we see the each 2-by-2 sub-matrix of the LHS and RHS of Equation (13) are the identical as claimed. □

A.2 MIMO convolution and transposed convolution

To extend our formulation to the MIMO case, we denote by $\boldsymbol{x} = (\boldsymbol{\xi}_1, \ldots, \boldsymbol{\xi}_C) \in \mathbb{R}^{C \times H \times W}$ a multi-channel signal.

MIMO convolution We let $\boldsymbol{W} = (\boldsymbol{w}_{11}, \ldots, \boldsymbol{w}_{1C}, \ldots, \boldsymbol{w}_{M1}, \ldots, \boldsymbol{w}_{MC}) \in \mathbb{R}^{M \times C \times 3 \times 3}$ be a multi-channel convolutional kernel of 3-by-3 filters, where C denotes the number of input channels and M denotes the number of output channels. The MIMO convolution is defined as

$$\mathrm{Conv}(\boldsymbol{W}, \boldsymbol{x}) = \sum_{c=1}^{C} (\boldsymbol{w}_{1c} * \boldsymbol{\xi}_c, \ldots, \boldsymbol{w}_{Mc} * \boldsymbol{\xi}_c) \in \mathbb{R}^{M \times H \times W}.$$

MIMO transposed convolution Let $\boldsymbol{x} = (\boldsymbol{\xi}_1, \ldots, \boldsymbol{\xi}_C) \in \mathbb{R}^{C \times H \times W}$ be a multi-channel signal. We let $\boldsymbol{V} = (\boldsymbol{v}_{11}, \ldots, \boldsymbol{v}_{1C}, \ldots, \boldsymbol{v}_{M1}, \ldots, \boldsymbol{v}_{MC}) \in \mathbb{R}^{M \times C \times 2 \times 2}$ be a multi-channel convolutional kernel of 2-by-2 filters. The MIMO transposed convolution is defined as

$$\mathrm{TConv}(\boldsymbol{V}, \boldsymbol{x}) = \sum_{c=1}^{C} (\boldsymbol{\xi}_c \otimes \bar{\boldsymbol{v}}_{1c}, \ldots, \boldsymbol{\xi}_c \otimes \bar{\boldsymbol{v}}_{Mc}) \in \mathbb{R}^{M \times 2H \times 2W}.$$

A.3 Up-block

An up-block receives multi-channel inputs from (i) low-resolution features in the shape of $(2C, H, W)$ and (ii) skip-connection features in the shape of $(C, 2H, 2W)$. With these input features, an up-block applies a transposed convolution to low-resolution features that halves the number of channels, concatenates the resulting features with skip-connection features, and then submits the concatenated results for another convolution. This can be written as

$$\begin{aligned}\mathrm{Up}_{\boldsymbol{W},\boldsymbol{V}} : \mathbb{R}^{C\times 2H\times 2W} \times \mathbb{R}^{2C\times H\times W} &\to \mathbb{R}^{C\times 2H\times 2W}\\ (\boldsymbol{\beta}, \boldsymbol{x}) &\mapsto \mathrm{Conv}([\boldsymbol{\beta}; \mathrm{TConv}(\boldsymbol{x}, \boldsymbol{V})], \boldsymbol{W}),\end{aligned}$$

where $\boldsymbol{W} \in \mathbb{R}^{2C\times C\times 3\times 3}$ and $\boldsymbol{V} \in \mathbb{R}^{2C\times C\times 2\times 2}$ are parameters and [;] denotes channel-wise concatenation.

A.4 The decoder dictionary

We define a linear map $g_{\tilde{\boldsymbol{\gamma}}}$ parametrized by $\tilde{\boldsymbol{\gamma}} \coloneqq \{\boldsymbol{W}_i, \boldsymbol{V}_i\}_{i=1}^{L}$ as

$$\begin{aligned}g_{\tilde{\boldsymbol{\gamma}}} : \mathbb{R}^{C\times H\times W} \times \cdots \times \mathbb{R}^{C/2^L\times 2^L\cdot H\times 2^L\cdot W} &\to \mathbb{R}^{C/2^L\times 2^L\cdot H\times 2^L\cdot W}\\ (\boldsymbol{\alpha}^{(0)}, \cdots, \boldsymbol{\alpha}^{(L)}) &\mapsto \boldsymbol{x}^{(L)},\end{aligned}$$

where

$$\boldsymbol{x}^{(i)} = \mathrm{Up}_{\boldsymbol{W}^{(i)},\boldsymbol{V}^{(i)}}(\boldsymbol{\alpha}^{(i)}, \boldsymbol{x}^{(i-1)})$$

for $i = 1, \dots L$, with L being the number of resolution levels (= 4 throughout this paper) and $\boldsymbol{x}^{(0)} = \boldsymbol{\alpha}^{(0)}$.

Here, the function $g_{\tilde{\boldsymbol{\gamma}}}$ transforms the sparse code to a tensor of the shape $\mathbb{R}^{C/2^L\times 2^L\cdot H\times 2^L\cdot W}$. Since our desired outputs are grey-scale or colored images in $\mathbb{R}^{1\times 2^L\cdot H\times 2^L\cdot W}$ or $\mathbb{R}^{3\times 2^L\cdot H\times 2^L\cdot W}$, we use an additional 1×1 convolution operator $\mathcal{T}_{\boldsymbol{K}}$ with parameters $\boldsymbol{K}$ to synthesize these features into a tensor with channel number 1 or 3. A decoder dictionary is defined as a composition of $g_{\tilde{\boldsymbol{\gamma}}}$ and $\mathcal{T}_{\boldsymbol{K}}$:

$$\boldsymbol{D}_{\boldsymbol{\gamma}} = \mathcal{T}_{\boldsymbol{K}} \circ g_{\tilde{\boldsymbol{\gamma}}},$$

where $\boldsymbol{\gamma} = \tilde{\boldsymbol{\gamma}} \cup \{\boldsymbol{K}\}$.

Appendix B Power iteration

Let $\boldsymbol{D}_{\boldsymbol{\gamma}}$ be a dictionary with parameters $\boldsymbol{\gamma}$. The dominant eigenvalue of $\boldsymbol{D}_{\boldsymbol{\gamma}}^{\top}\boldsymbol{D}_{\boldsymbol{\gamma}}$ can be approximately derived by first estimating the eigenvector associated with the dominant eigenvalue using the power iteration method, by recursively calculating

$$\boldsymbol{b}_{k+1} = \frac{\boldsymbol{D}_{\boldsymbol{\gamma}}^{\top}\boldsymbol{D}_{\boldsymbol{\gamma}}\boldsymbol{b}_k}{\left\|\boldsymbol{D}_{\boldsymbol{\gamma}}^{\top}\boldsymbol{D}_{\boldsymbol{\gamma}}\boldsymbol{b}_k\right\|} \tag{16}$$

up to some step K. The estimated dominant eigenvalue can then be derived from

$$\lambda_K = \frac{\boldsymbol{b}_K^{\top}\boldsymbol{D}_{\boldsymbol{\gamma}}^{\top}\boldsymbol{D}_{\boldsymbol{\gamma}}\boldsymbol{b}_K}{\boldsymbol{b}_K^{\top}\boldsymbol{b}_K}. \tag{17}$$

Appendix C Details of experimental setup

In Table 8 and Table 9 we summarize the hyperparameters used for training Classic U-Net and ISTA U-Net.

Task	Epoch number	Batch size	Crop size	Learning rate	Loss function
Super-resolution	1000	32	64	0.001	YCbCr-MSE
Ellipsoid phantoms	50	4	-	0.001	MSE
Lodopab-CT	20	32	-	0.001	MSE
fastMRI	50	8	-	0.001	MSE

Table 8: **Hyperparameters used for the classic U-Net.**

Task	Epoch number	Batch size	Crop size	Learning rate	Loss function	Num ISTA steps	Lasso parameter	Rectified output
Super-resolution	1000	8	64	2×10^{-4}	YCbCr-MSE	10	0.01	True
Ellipsoid phantoms	50	4	-	2×10^{-4}	MSE	10	0.001	False
Lodopab-CT	20	2	-	2×10^{-4}	MSE	5	0.001	True
fastMRI	20	2	-	5×10^{-5}	MSE	5	0.001	False

Table 9: **Hyperparameters used for the ISTA U-Net.**

For the image super-resolution task, following the convention, we converted RGB-valued model outputs to YCbCr values and used the Y-th channel for evaluation. For this reason, we used the YCbCr-MSE loss, which is defined by weighting channels of RGB-valued model outputs and channels of their respective RGB-valued targets in accordance with their contributions to the Y-th channel of YCbCr-valued images.

In Table 9, the values in the rectified output column refer to whether we attach a ReLU function to generate outputs or not—the rectifier is helpful if target values are non-negative.

Appendix D The sparseness of the representation learned by the U-Net and the ISTA U-Net

In this section, we compare the sparseness of representations of the U-Net and the ISTA U-Net through the compressibility of their feature maps. Signal compressibility is a concept more general than sparseness: While a signal is said to be sparse with respect to a dictionary if the signal's coefficients in that dictionary have few non-zero entries, it is said to be compressible if the magnitudes of the coefficients exhibit a power-law decay rate. We find that the compressibility of the U-Net and the ISTA U-Net are in excellent agreement (Figure 6), especially over the ellipsoid phantom, Lodopab-CT, and fastMRI datasets; on the super-resolution problem (the Set-5 dataset), the agreement is not as close but the general trend persists.

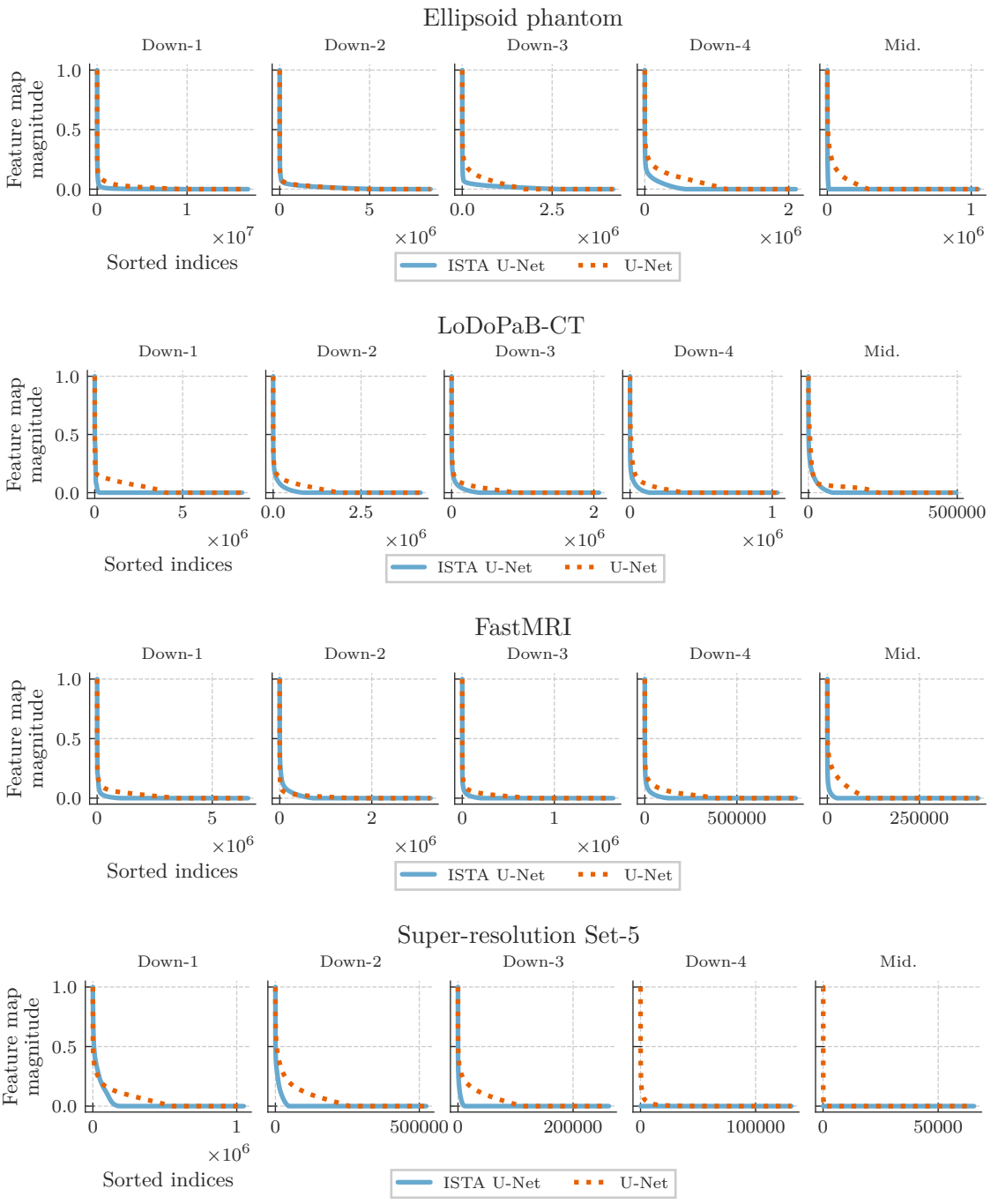

Figure 6: **Compressibility of U-Net and ISTA U-Net feature maps.** Each row corresponds to a dataset. Each panel in a row corresponds to a feature-map resolution level in the U-Net and ISTA U-Net's down-sampling path, from the shallowest layer (Down-1) to the deepest layer (Mid.). In each panel, feature map magnitudes are normalized to be from 0 to 1. We observe that convolutional feature maps of the U-Net and the ISTA U-Net are similarly compressible in the sense that the sorted magnitudes of the feature map magnitudes decay at a similar rate.

References

Adler, J. and Öktem, O. Solving ill-posed inverse problems using iterative deep neural networks. *Inverse Problems*, 33(12):124007, Nov 2017.

Adler, J. and Öktem, O. Learned primal-dual reconstruction. *IEEE Transactions on Medical Imaging*, 37(6):1322–1332, 2018.

Baguer, D. O., Leuschner, J., and Schmidt, M. Computed tomography reconstruction using deep image prior and learned reconstruction methods. *Inverse Problems*, 36(9):094004, Sep 2020.

Bevilacqua, M., Roumy, A., Guillemot, C., and Morel, M. Low-complexity single-image super-resolution based on nonnegative neighbor embedding. In *Proceedings of the British Machine Vision Conference*, pp. 135.1–135.10. BMVA Press, 2012.

Bristow, H., Eriksson, A., and Lucey, S. Fast convolutional sparse coding. In *2013 IEEE Conference on Computer Vision and Pattern Recognition*, pp. 391–398, 2013.

Bruna, J. and Mallat, S. Invariant scattering convolution networks. *IEEE Transactions on Pattern Analysis and Machine Intelligence*, 35(8):1872–1886, 2013.

Candes, E. J., Romberg, J., and Tao, T. Robust uncertainty principles: Exact signal reconstruction from highly incomplete frequency information. *IEEE Transactions on Information Theory*, 52 (2):489–509, 2006.

Chambolle, A. An algorithm for total variation minimization and applications. *Journal of Mathematical Imaging and Vision*, 20(1–2):89–97, January 2004.

Charlety, J., Voronin, S., Nolet, G., Loris, I., Simons, F. J., Sigloch, K., and Daubechies, I. C. Global seismic tomography with sparsity constraints: Comparison with smoothing and damping regularization. *Journal of Geophysical Research: Solid Earth*, 118(9):4887–4899, 2013.

Chen, C. and Donoho, D. Basis pursuit. In *Proceedings of 1994 28th Asilomar Conference on Signals, Systems and Computers*, volume 1, pp. 41–44 vol.1, 1994.

Chen, H., Zhang, Y., Kalra, M. K., Lin, F., Chen, Y., Liao, P., Zhou, J., and Wang, G. Low-dose CT with a residual encoder-decoder convolutional neural network. *IEEE Transactions on Medical Imaging*, 36(12):2524–2535, 2017.

Daubechies, I., Defrise, M., and Mol, C. D. An iterative thresholding algorithm for linear inverse problems with a sparsity constraint. *Communications on Pure and Applied Mathematics*, 57(11): 1413–1457, 2004.

Dong, C., Loy, C. C., He, K., and Tang, X. Image super-resolution using deep convolutional networks. *IEEE Transactions on Pattern Analysis and Machine Intelligence*, 38(2):295–307, 2016.

Donoho, D. L. Compressed sensing. *IEEE Transactions on information theory*, 52(4):1289–1306, 2006.

Elad, M. *Sparse and Redundant Representations: From Theory to Applications in Signal and Image Processing*. Springer Publishing Company, Incorporated, 1st edition, 2010.

Elad, M. and Aharon, M. Image denoising via sparse and redundant representations over learned dictionaries. *IEEE Transactions on Image Processing*, 15(12):3736–3745, 2006.

Etmann, C., Ke, R., and Schönlieb, C.-B. iUNets: Fully invertible U-nets with learnable up- and downsampling, 2020.

Gu, S., Zuo, W., Xie, Q., Meng, D., Feng, X., and Zhang, L. Convolutional sparse coding for image super-resolution. In *2015 IEEE International Conference on Computer Vision (ICCV)*, pp. 1823–1831, 2015.

Han, Y. and Ye, J. C. Framing U-Net via deep convolutional framelets: Application to sparse-view CT. *IEEE Transactions on Medical Imaging*, 37(6):1418–1429, 2018.

He, J., Wang, Y., and Ma, J. Radon inversion via deep learning. *IEEE Transactions on Medical Imaging*, 39(6):2076–2087, 2020.

Huang, J.-B., Singh, A., and Ahuja, N. Single image super-resolution from transformed self-exemplars. In *Proceedings of the IEEE Conference on Computer Vision and Pattern Recognition*, pp. 5197–5206, 2015.

Hyun, C. M., Kim, H. P., Lee, S. M., Lee, S., and Seo, J. K. Deep learning for undersampled MRI reconstruction. *Physics in Medicine & Biology*, 63(13):135007, June 2018.

Jin, K. H., McCann, M. T., Froustey, E., and Unser, M. Deep convolutional neural network for inverse problems in imaging. *IEEE Transactions on Image Processing*, 26(9):4509–4522, 2017.

Kim, J., Lee, J. K., and Lee, K. M. Accurate image super-resolution using very deep convolutional networks. In *2016 IEEE Conference on Computer Vision and Pattern Recognition (CVPR)*, pp. 1646–1654, 2016.

Kothari, K., Gupta, S., v. de Hoop, M., and Dokmanić, I. Random mesh projectors for inverse problems. In *International Conference on Learning Representations*, 2019.

Lai, W., Huang, J., Ahuja, N., and Yang, M. Deep laplacian pyramid networks for fast and accurate super-resolution. In *IEEE Conference on Computer Vision and Pattern Recognition*, 2017.

Lecouat, B., Ponce, J., and Mairal, J. A flexible framework for designing trainable priors with adaptive smoothing and game encoding. In *Proceedings of Neural Information Processing Systems (NeurIPS)*, 2020.

Leuschner, J. Deep inversion validation library. https://github.com/jleuschn/dival, 2020.

Leuschner, J., Schmidt, M., Baguer, D. O., and Maaß, P. The LoDoPaB-CT dataset: A benchmark dataset for low-dose CT reconstruction methods, 2019.

Liebgott, H., Prost, R., and Friboulet, D. Pre-beamformed RF signal reconstruction in medical ultrasound using compressive sensing. *Ultrasonics*, 53(2):525 – 533, 2013.

Lim, B., Son, S., Kim, H., Nah, S., and Lee, K. M. Enhanced deep residual networks for single image super-resolution. In *2017 IEEE Conference on Computer Vision and Pattern Recognition Workshops (CVPRW)*, pp. 1132–1140, 2017.

Lustig, M., Donoho, D. L., Santos, J. M., and Pauly, J. M. Compressed sensing MRI. *IEEE signal processing magazine*, 25(2):72–82, 2008.

Mairal, J., Bach, F., and Ponce, J. Task-driven dictionary learning. *IEEE Transactions on Pattern Analysis and Machine Intelligence*, 34(4):791–804, April 2012.

Mallat, S. Group invariant scattering. *Communications on Pure and Applied Mathematics*, 65(10): 1331–1398, 2012.

Martin, D., Fowlkes, C., Tal, D., and Malik, J. A database of human segmented natural images and its application to evaluating segmentation algorithms and measuring ecological statistics. In *Proceedings of the 8th International Conference on Computer Vision*, volume 2, pp. 416–423, July 2001.

Papyan, V., Romano, Y., and Elad, M. Convolutional neural networks analyzed via convolutional sparse coding. *Journal of Machine Learning Research*, 18(83):1–52, 2017.

Recht, M. P., Zbontar, J., Sodickson, D. K., Knoll, F., Yakubova, N., Sriram, A., Murrell, T., Defazio, A., Rabbat, M., Rybak, L., Kline, M., Ciavarra, G., Alaia, E. F., Samim, M., Walter, W. R., Lin, D. J., Lui, Y. W., Muckley, M., Huang, Z., Johnson, P., Stern, R., and Zitnick, C. L. Using deep learning to accelerate knee MRI at 3T: results of an interchangeability study. *American Journal of Roentgenology*, pp. 1–9, October 2020.

Ronneberger, O., Fischer, P., and Brox, T. U-net: Convolutional networks for biomedical image segmentation. In Navab, N., Hornegger, J., Wells, W. M., and Frangi, A. F. (eds.), *Medical Image Computing and Computer-Assisted Intervention – MICCAI 2015*, pp. 234–241. Springer International Publishing, 2015.

Schulter, S., Leistner, C., and Bischof, H. Fast and accurate image upscaling with super-resolution forests. In *2015 IEEE Conference on Computer Vision and Pattern Recognition (CVPR)*, pp. 3791–3799, 2015.

Shepp, L. A. and Logan, B. F. The fourier reconstruction of a head section. *IEEE Transactions on Nuclear Science*, 21(3):21–43, 1974.

Tibshirani, R. Regression shrinkage and selection via the Lasso. *Journal of the Royal Statistical Society: Series B (Methodological)*, 58(1):267–288, 1996.

Timofte, R., Smet, V. D., and Gool, L. V. A+: Adjusted anchored neighborhood regression for fast super-resolution. In Cremers, D., Reid, I., Saito, H., and Yang, M. (eds.), *Computer Vision – ACCV 2014*, pp. 111–126. Springer International Publishing, 2015.

Yang, J., Wright, J., Huang, T. S., and Ma, Y. Image super-resolution via sparse representation. *IEEE Transactions on Image Processing*, 19(11):2861–2873, 2010.

Ye, J. C. and Sung, W. K. Understanding geometry of encoder-decoder CNNs. In Chaudhuri, C. and Ruslan, S. (eds.), *Proceedings of the 36th International Conference on Machine Learning, ICML 2019, 9-15 June 2019, Long Beach, California, USA*, volume 97 of *Proceedings of Machine Learning Research*, pp. 7064–7073. PMLR, 2019.

Ye, J. C., Han, Y., and Cha, E. Deep convolutional framelets: A general deep learning framework for inverse problems. *SIAM Journal on Imaging Sciences*, 11(2):991–1048, 2018.

Yin, R., Gao, T., Lu, Y. M., and Daubechies, I. A tale of two bases: Local-nonlocal regularization on image patches with convolution framelets. *SIAM Journal on Imaging Sciences*, 10(2):711–750, 2017.

Zarka, J., Thiry, L., Angles, T., and Mallat, S. Deep network classification by scattering and homotopy dictionary learning. In *International Conference on Learning Representations*, 2020.

Zbontar, J., Knoll, F., Sriram, A., Muckley, M. J., Bruno, M., Defazio, A., Parente, M., Geras, K. J., Katsnelson, J., Chandarana, H., Zhang, Z., Drozdzal, M., R., A., Rabbat, M., Vincent, P., Pinkerton, J., Wang, D., Yakubova, N., Owens, E., Zitnick, C. L., Recht, M. P., Sodickson, D. K., and Lui, Y. W. fastMRI: An open dataset and benchmarks for accelerated MRI. *ArXiv e-prints*, 2018.

Zeyde, R., Elad, M., and Protter, M. On single image scale-up using sparse-representations. In *Proceedings of the 7th International Conference on Curves and Surfaces*, pp. 711–730, Berlin, Heidelberg, 2010. Springer-Verlag.